traviolet plus PR favored a repair process beneficial to survival. Either age damage was corrected at the time of treatment and was inherited as reduced levels of DNA damage in progeny cells, or the treatment activated a process that persisted for some cell divisions after treatment.

Evidence is available that DNA damage accumulates in aged cells of higher organisms because of defective repair capacity (*12*). Mechanisms proposed for reduced repair in aged cells include decreased levels of DNA polymerases, loss of fidelity of DNA polymerase, or changes in the DNA-chromatin complex, reducing the accessibility of DNA lesions to repair (*13*). Ultraviolet plus PR may function to counteract such age changes in repair, or interact with some yet unknown contributor to repair capacity. Differences in repair capacity correlate with organismal life-span (*14, 15*). Cell life-span may be a reflection of the genetic needs for mutation frequencies (*16, 17*), and thus regulation of repair becomes a fundamental life maintenance and aging mechanism. Multicellular organisms can be expected to conserve the aging and life maintenance processes of eukaryote cells, since the evolution of multicellular organisms was relatively short in comparison to the long period of evolution of eukaryotes (*17*). Different cells within the same organism have different repair capacities (*13, 18*). If cell life-span determines organismal life-span (*6*), the cells with the shortest life-span (the weakest link) will determine the life-span of the whole organism, if it is assumed that the cells are essential for survival and cannot be replaced. The weakest link can be expected to differ in different species. The symptoms of aging manifested by consequences of loss of function of a particular organ should be diverse (*19*). The above results provide an explanation for the findings that organismal life-span is correlated with repair capacity of cells (*14, 15*). Exceptions would be expected because of the complexity of the repair processes, variants within species, and species whose life-span is not determined by cellular mutational deterioration. DNA damage is linked not only to clonal senescence but also to carcinogenesis (*20*). Ultraviolet-induced damage resulted in tumorigenesis in fish but not when the damage was repaired by photoreactivation (*21*).

Accordingly, age damage can be reversed or delayed. An understanding of the molecular mechanisms underlying this biological result could illuminate other means to activate the repair system. If higher organisms have maintained a reserve repair capacity, activation should lead to reduction in mutagenesis and degenerative diseases in higher organisms. The results provide a new approach for regulation and reduction of mutation frequency: the activation of a reserve repair or protection process.

JOAN SMITH-SONNEBORN

Department of Zoology and Physiology, University of Wyoming, Laramie 82071

References and Notes

1. T. M. Sonneborn, *J. Protozool.* **1**, 38 (1954).
2. J. Smith-Sonneborn, *J. Radiat. Res.* **46**, 64 (1971).
3. B. M. Sutherland, W. L. Carrier, R. B. Setlow, *Science* **158**, 1699 (1967).
4. S. Rodermel and J. Smith-Sonneborn, *Genetics* **87**, 259 (1977).
5. T. M. Sonneborn and M. Schneller, in *Biology of Aging*, B. L. Strehler, Ed. (Waverly, Baltimore, 1960), p. 286.
6. L. Hayflick, *BioScience* **25**, 629 (1975).
7. R. W. Siegel, *Exp. Cell Res.* **24**, 6 (1961).
8. Daily isolation lines were initiated with a single fertilized cell in a separate depression. The next day, the number of cells was counted and one passed to a new depression. The daily fission rate was determined by the $\log_2$ of the number of cells derived from a single cell. The procedure of counting and reisolation is repeated daily and expanded to several sublines when desired. The genetic markers used to monitor aging lines for maintenance of the heterozygous phenotype in experiments 1, 2, and 3 included malate dehydrogenase codominant alleles (T. Williams and J. Smith-Sonneborn, unpublished) and trichocyst discharge ability (kindly supplied by D. Nyberg, University of Illinois). (Those sublines without the heterozygous phenotype were eliminated since they were interpreted to be lines which underwent illicit autogamy.)
9. Ultraviolet was given to synchronized cells $1^1/_2$ hours after cell division in microdrops of food diluted immediately after treatment with fresh food. Single cells alive the following day were maintained in sublines and carried in isolation lines.
10. A germicidal lamp emitting mainly at 254 nm supplied the ultraviolet at a rate of 180 to 540 J/m^2. Photoreactivation was as described in (*2*) and (*4*).
11. W. J. Dixon and F. J. Massey, Jr., in *Introduction to Statistical Analysis* (McGraw-Hill, New York, 1957).
12. S. P. Modak and G. B. Price, *Exp. Cell Res.* **65**, 289 (1971); G. B. Price, S. P. Modak, T. Makinodan, *Science* **171**, 917 (1971); D. W. Appelby and S. P. Modak, *Proc. Natl. Acad. Sci. U.S.A.* **74**, 5579 (1977).
13. S. P. Modak and C. Unger-Ullmann, in *Results and Problems of Cell Differentiation*, W. Beermann, W. J. Gehring, J. B. Gurdon, F. C. Kafatos, J. Reinert, Eds. (Springer-Verlag, New York, in press).
14. R. W. Hart and R. B. Setlow, *Proc. Natl. Acad. Sci. U.S.A.* **71**, 2169 (1974).
15. G. A. Sacher and R. W. Hart, *Birth Defects Orig. Artic. Ser.* **14**, 71 (1978).
16. J. E. Trosko and R. Hart, *Interdiscip. Top. Gerontol.* **9**, 168 (1978); R. W. Hart and J. E. Trosko, *ibid.*, p. 134.
17. L. Margolis, *Origin of Eukaryotic Cells* (Yale Univ. Press, New Haven, Conn., 1970); R. J. Cutler, *Interdiscip. Top. Gerontol.* **9**, 83 (1978).
18. H. B. Jones, *Proc. Health Phys. Soc.* (1956), p. 114.
19. R. W. Hart, R. B. Setlow, R. E. Gibson, T. L. Hoskins, *Abstracts of the 10th International Congress on Gerontology*, Jerusalem, 1975.
20. R. W. Hart and J. Smith-Sonneborn, *Abstracts of the 11th International Congress on Gerontology*, Tokyo, Japan, August 1978.
21. R. W. Hart, R. B. Setlow, A. Woodhead, *Proc. Natl. Acad. Sci. U.S.A.* **74**, 5574 (1977).
22. I thank Dr. R. W. Hart, Ohio State University, for his stimulating discussion and encouragement and review of drafts of this manuscript; Professor T. M. Sonneborn, Indiana University, for his comments and review; Dr. L. McDonald for statistical consulation; P. Hanson, D. Millhouse, and E. VanKirk for isolating more than 10,000 cells in the dark over a 6- to 9-week interval, and T. Williams for the electrophoretic patterns of MDH. Supported in part by DOE contract EE 77-5-0204477-A000 and NSF grant PCM77 04315.

4 August 1978; revised 3 November 1978

Polyoma Virion and Capsid Crystal Structures

Abstract. *X-ray diffraction shows that complete virus particles and empty capsids crystallize isomorphously. The surface morphology of the protein coat, as revealed by electron microscopy, is the dominant structural feature determining the intensity of x-ray reflections to a resolution of approximately 30 angstroms. The structure and variability of the viral chromatin core can now be analyzed by comparison of electron density maps.*

Polyoma virus DNA, and that of the similar tumorogenic simian virus 40, is packaged inside an icosahedral capsid as a supercoiled, circular, double-stranded molecule that is complexed with cellular histones (*1*). Infected cells also produce empty, noninfectious capsids whose surface morphology is very similar to that of the complete virion (*2*). The capsid is built of 72 morphological units arranged on an icosahedral surface lattice with triangulation number T = 7 (dextro) (*3*). Polyoma virions and capsids have previously been crystallized from ammonium sulfate (*4*). Using sodium sulfate, we have now obtained large, single crystals suitable for x-ray structure analysis.

Sodium rather than ammonium sulfate was chosen for comparative electron microscopic studies of glutaraldehyde-fixed crystals to avoid reaction with ammonia. Glutaraldehyde fixation also proved convenient for neutralizing the infectivity of the virion crystals used for studies in our x-ray laboratory, which does not yet have facilities for virus containment. Purified virions and capsids (*5*) were crystallized by the hanging drop method (*6*) from half-saturated sodium sulfate. Rhombic dodecahedral crystals (the same form obtained from ammonium sulfate) grow up to 0.5 mm across in about 1 week. Large crystals ($\lesssim$1 mm) often have highly stellated vertices. Virion crystals have better-developed faces and sharper edges than capsid crystals.

X-ray precession photographs (Fig. 1, a to c) show that the particles in the crystals are arranged on a body-centered

0036-8075/79/0316-1117$00.50/0

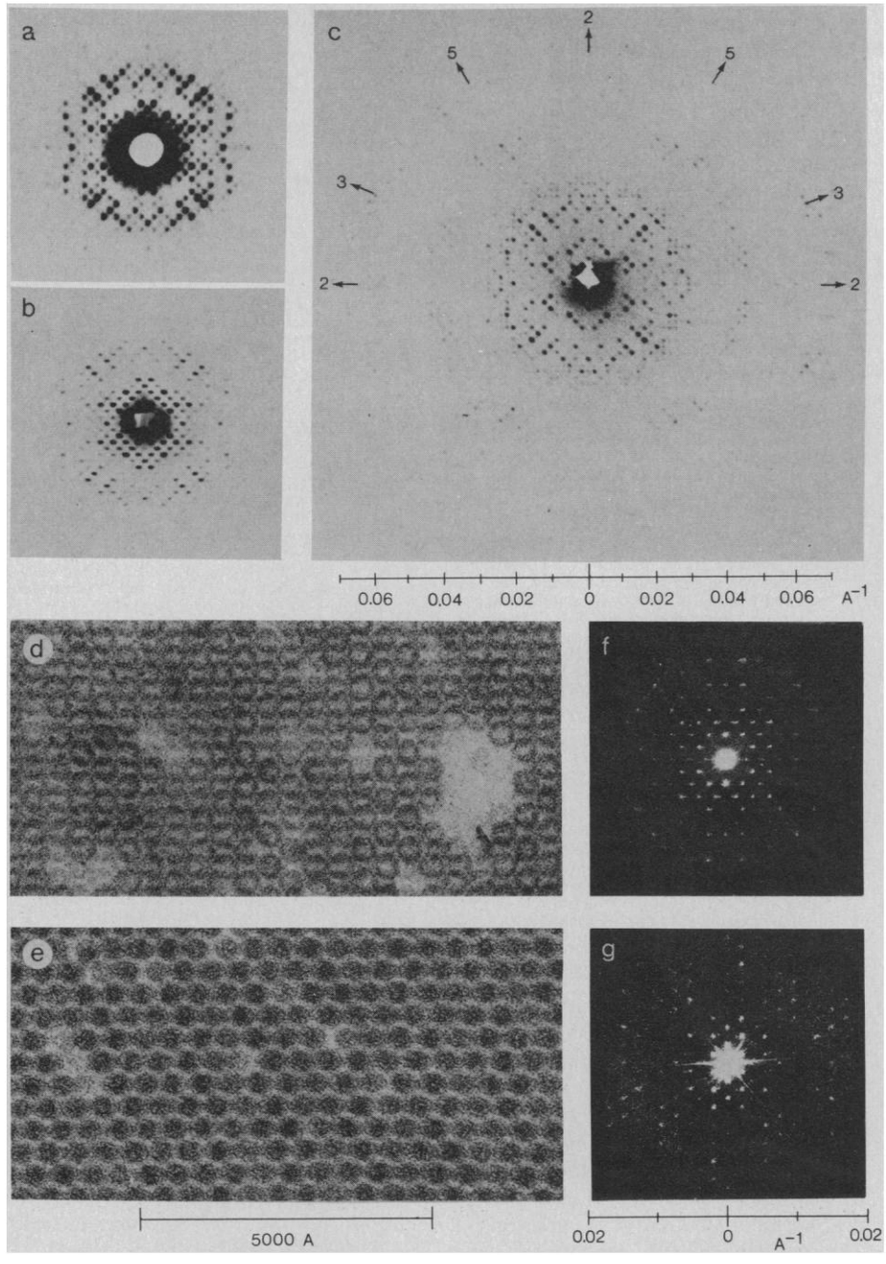

Fig. 1. (a to c) Precession x-ray diffraction photographs of virion and capsid crystals viewed along the [100] direction with cube axes oriented vertical and horizontal. The scale for these three patterns is marked in (c). Exposures were made for 2 to 3 days, using a double-mirror focusing camera with an order-to-order resolution of 1000 to 1500 Å and an Elliott GX-6 rotating anode x-ray generator. The capsid crystal in (a) and the virion crystal in (b) have comparable short-range disorder, but the virion crystal in (c) is better ordered. Arrows in (c) mark the directions of the icosahedral two-, three-, and fivefold axes that lie in the plane of these diffraction patterns. (d and e) Electron micrographs of thin sections of crystals fixed with glutaraldehyde and osmium and embedded in Epon; (f and g) optical diffraction patterns of these micrographs. Scales for the micrographs and optical patterns, respectively, are marked at the bottom. Capsid crystal sections in (d) and (e) are cut approximately normal to a [110] direction. In (d) the lattice is oriented with a [001] axis vertical; the [110] axis near the direction of view is tilted by 8° sideways from the normal to the plane of sectioning. This section shows a diagonal layer from the body-centered cubic lattice in which the nearest-neighbor separation is about 480 Å. The virion crystal in (e) is oriented with a [1$\bar{1}$0] axis nearly vertical, and the direction of view, normal to the section, is between the [110] and [111] axes. Horizontal rows of virions in (e) are spaced 395 Å apart, which is the same as the spacing of vertical columns of capsids in (d). Optical diffraction patterns of both capsid (f) and virion (g) micrographs show that the resolution is about 50 Å. Because the sections are only about one particle thick and are slightly oblique to principal planes of the lattice, some spots appear in the optical diffraction patterns that do not occur in the x-ray patterns of crystals viewed along the [110] direction.

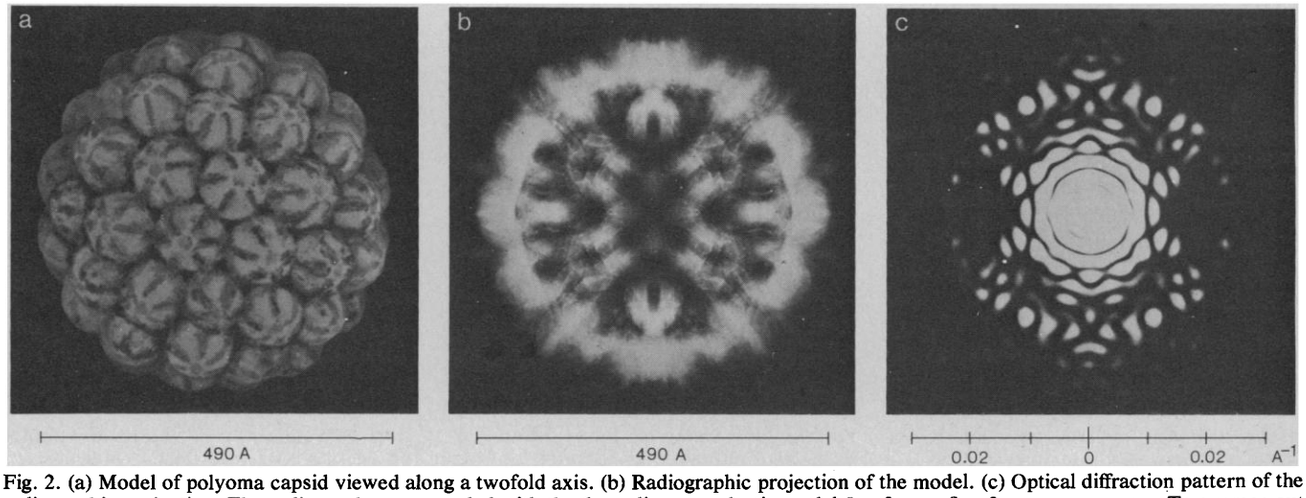

Fig. 2. (a) Model of polyoma capsid viewed along a twofold axis. (b) Radiographic projection of the model. (c) Optical diffraction pattern of the radiographic projection. The radiograph was recorded with the 6-cm-diameter plastic model 5 m from a fine-focus x-ray source. To average out small irregularities in the model, the radiograph was superimposed on itself with the *m m* symmetry of the icosahedral twofold projection. The optical diffraction pattern (c) provides an analog continuous transform of the capsid model corresponding to the sampled transform of the x-ray patterns (Fig. 1, a to c) from capsid and virion crystals viewed down the [100] axis.

cubic latice. The lattice constant a of the cubic unit cell in virion crystals is 568 ± 4 Å; for capsid crystals this dimension is about 1 percent smaller. The distance between neighboring lattice points of these body-centered crystals is $(\sqrt{3}/2)a$, or about 490 Å, which is close to the particle packing diameter measured by electron microscopy (Fig. 1, d and e). The space group of the crystal [*I*23] requires that each lattice point have tetrahedral [23] symmetry. Particle centers lie on lattice points of the crystal, with twofold and threefold particle axes coincident with crystal symmetry axes. Icosahedral [532] point group symmetry of the particle is reflected by spikes of high intensity in the diffraction pattern that lie in the direction of the noncrystallographic symmetry axes (for example, Fig. 1c). The particle and space group symmetry is the same as that of tomato bushy stunt virus (TBSV) (*7*), but the polyoma virus crystal unit cell has three times the volume of the TBSV cell. The data collection strategy developed for TBSV (*8*) can be used with polyoma virus crystals, but for a particular resolution three times as many data must be collected.

The resolution (*9*) at which the polyoma virus diffraction patterns fade out is not the same for all crystals. The most highly ordered crystal examined showed reflections (in a still photograph) out to a spacing of 6.5 Å. In the screenless precession photograph of a well-ordered virion crystal (Fig. 1c), upper level spots with a spacing of 15 Å are clearly visible. For the few capsid crystals (Fig. 1a) photographed, and for some virion crystals (Fig. 1b), diffraction beyond a resolution of 30 Å was not observed. An osmium-fixed and Epon-embedded crystal diffracted to a resolution of only about 40 Å.

The small-angle x-ray reflections from the well-ordered virion crystal (Fig. 1c) are weak, whereas the corresponding reflections from the capsid crystal (Fig. 1a), and from the virion crystal with comparable short-range disorder (Fig. 1b), are relatively strong. Differences in the intensity of the reflections from virion and capsid crystals must result, at least in part, from the scattering contribution of the viral chromatin core. We cannot yet determine whether the intensity variations observed among virion crystals are due to differences in composition or conformation.

Electron micrographs of selected thin crystal sections, cut nearly normal to principal crystallographic directions, directly reveal the particle packing arrangement deduced from the x-ray diffraction patterns. In sections about one particle thick the capsids appear hollow (Fig. 1d), whereas the virions have a solid core (Fig. 1e). The center-to-center, nearest-neighbor separation of particles in the plane of the sections is about 480 Å.

Vacancies, which are a characteristic feature of these crystals, give the sections a moth-eaten appearance. The holes are generally larger and more frequent in capsid than in virion crystals. Abnormally shaped particles [presumably polymorphic assemblies of capsid subunits (*2*)] are often observed at the edges of vacancies. Inclusion of aberrant particles necessarily disrupts the lattice order locally; but the disorganization does not propagate over long distances. Vacancies diffract, by Babinet's principle, like ghosts of the particles that would have filled up the holes. Randomly distributed vacancies will therefore diffract like a solution of the missing particles. Still photographs of capsid crystals do, in fact, show diffuse small-angle scattering similar to the solution scattering pattern.

Spherically symmetric small-angle scattering from virion solutions corresponds to that from a solid sphere of diameter 490 Å, but the scattering from capsids indicates an empty shell with an inside diameter of about 300 Å. Nonspherically symmetric scattering from virion solutions has been accounted for to a resolution of ~60 Å by a simple point model (*10*) representing the arrangement of bumps on the capsid surface seen by electron microscopy.

Finch (*11*) reconstructed a three-dimensional image of polyoma virus to a resolution of 25 Å from electron micrographs of negatively stained particles. We have produced diffraction patterns from a model of this structure as an analog for analyzing the low-resolution x-ray diffraction patterns. The model used was originally built (*12*) to fit electron micrographs of negatively stained human wart virus (*13*); it also corresponds closely to the polyoma virus morphology revealed by Finch's reconstruction. Optical diffraction (Fig. 2c) from a radiographic projection (Fig. 2b) of the model (Fig. 2a) provides the analog Fourier transform. Although the optical processes introduce nonlinearities that distort the amplitude scale of the transform, the intensity distributions in the optical (Fig. 2c) and x-ray (Fig. 1, a to c) diffraction patterns correspond relatively well.

A close correlation between information about virus structure from x-ray diffraction and that from electron microscopy has been established for TBSV to a resolution of ~30 Å (*14*). A qualitatively similar correlation can be made for polyoma virus. The 72 bumps on the surface of the polyoma capsid that result from the clustering into pentamers and hexamers of the 420 protein subunits produce a strong modulation in the Fourier transform of the model at a spacing of ~50 Å. The intensity distribution in the x-ray diffraction patterns of virion and capsid crystals in this region is similar to that in the optical diffraction pattern from the capsid model. This indicates that the bumps in the capsid surface revealed by electron microscopy are the dominant feature determining the intensity of the diffraction out to a resolution of ~30 Å.

The design principles (*15*) applied in the construction of the T = 7 polyoma capsid are the same as those used for smaller icosahedral viruses. High-resolution density maps of the TBSV coat protein structure have revealed how quasi-equivalent packing of the 180 identical protein subunits in the T = 3 capsid is achieved (*16*). A similar crystallographic analysis of the southern bean mosaic virus (SBMV) structure is in progress (*17*). The genome of these small plant viruses is a single-stranded RNA molecule that is packaged as a relatively disordered coil inside a very regular capsid. In contrast, the DNA of polyoma virus and simian virus 40 forms a circular piece of chromatin (*18*) consisting of 20 or more nucleosomes, which must be closely packed within the capsid.

In infected cells, histone H1 stabilizes the unpackaged viral chromatin as a compact cluster of nucleosomes about 300 Å in diameter (*19, 20*). Up to 26 nucleosomes have been counted on the beaded ring formed when the minichromosome is unfolded (*20*). Possible mechanisms for orderly condensation of the beaded ring have been illustrated, but no direct information is yet available about the arrangement of nucleosomes within the cluster. This cluster could fit neatly within the 300-Å cavity of the capsid. It is therefore possible that the higher-order arrangement of the packaged ring of nucleosomes that lack histone H1 may be similar to that of the intracellular form that includes H1. Capsid proteins evidently serve a role analogous to that of H1 in stabilizing a compact nucleohistone core.

Changes in the chromatin structure within the capsid under different conditions could account for some of the variation observed in the intensities of small-angle x-ray reflections among virion crystals. Isomorphism of the protein

coat in all the virion and capsid crystals implies that the structure or structures of the chromatin core can be determined by Fourier methods. Phases for x-ray reflections can be calculated to a resolution of ~30 Å (*14*) from the particle shape determined by electron microscopy (*11*), and these phases can be refined by averaging about noncrystallographic symmetry axes (*21*) to produce three-dimensional maps of the electron density within the particle. The detail that can be resolved in the chromatin core will depend on the order in the condensed nucleosome cluster and its relation to the icosahedral symmetry of the capsid.

K. W. ADOLPH*
D. L. D. CASPAR
C. J. HOLLINGSHEAD
EATON E. LATTMAN†
W. C. PHILLIPS
Structural Biology Laboratory, Rosenstiel Basic Medical Sciences Research Center, Brandeis University, Waltham, Massachusetts 02154
W. T. MURAKAMI
Department of Biochemistry, Brandeis University

References and Notes

1. G. C. Fareed and D. Davoli, *Annu. Rev. Biochem.* **46**, 471 (1977).
2. J. T. Finch and L. V. Crawford, in *Comprehensive Virology*, H. Fraenkel-Conrat and R. R. Wagner, Eds. (Plenum, New York, 1975), vol. 5, p. 119.
3. A. Klug, *J. Mol. Biol.* **11**, 424 (1965).
4. W. T. Murakami, *Science* **142**, 56 (1963).
5. ——, R. Fine, M. R. Harrington, Z. Ben Sassan, *J. Mol. Biol.* **36**, 153 (1968).
6. A. McPherson, in *Methods of Biochemical Analysis*, D. Glick, Ed. (Academic Press, New York, 1977), vol. 23, p. 249.
7. D. L. D. Caspar, *Nature (London)* **177**, 476 (1956).
8. C. E. Shutt and F. K. Winkler, in *The Rotation Method in Crystallography*, U. Arndt and A. J. Wonacott, Eds. (North-Holland, Amsterdam, 1976), p. 173.
9. Resolution is defined by the spacing $d = \lambda/2\sin\theta$, where θ is the largest diffraction angle of the observed reflections and λ is the x-ray wavelength. Short-range disorder in the crystals can be idealized as random displacements of the particle centers from the points of the perfect lattice. The resolution at which the Bragg reflections fade out is proportional to the mean amplitude of these displacements. In the best-ordered crystal examined, the mean displacement of the particles is about 1 percent of the nearest-neighbor separation; at the other extreme, the short-range disorder in osmium-fixed crystals, as measured by both x-ray diffraction and electron microscopy, is about ten times greater.
10. A. Jack and S. C. Harrison, *J. Mol. Biol.* **99**, 15 (1975).
11. J. T. Finch, *J. Gen. Virol.* **24**, 359 (1974).
12. D. L. D. Caspar, *J. Mol. Biol.* **15**, 365 (1966).
13. A. Klug and J. T. Finch, *ibid.* **11**, 403 (1965).
14. A. Jack, S. C. Harrison, R. A. Crowther, *ibid.* **97**, 163 (1975).
15. D. L. D. Caspar and A. Klug, *Cold Spring Harbor Symp. Quant. Biol.* **27**, 1 (1962).
16. F. K. Winkler, C. E. Schutt, S. C. Harrison, G. Bricogne, *Nature (London)* **265**, 509 (1977); S. C. Harrison, A. J. Olson, C. E. Schutt, F. K. Winkler, G. Bricogne, *ibid.*, in press.
17. D. Suck, I. Rayment, J. E. Johnson, M. G. Rossmann, *Virology* **85**, 187 (1978).
18. J. D. Griffith, *Science* **187**, 1202 (1975); J. E. Germond, B. Hirt, P. Oudet, M. Gross-Bellard, P. Chambon, *Proc. Natl. Acad. Sci. U.S.A.* **72**, 1843 (1975).
19. G. Christiansen and J. D. Griffith, *Nucleic Acids Res.* **4**, 1837 (1977); A. J. Varshavsky, S. A. Nedospasov, V. V. Schmatchenko, Y. V. Bakayev, P. M. Shumackov, G. P. Georgiev, *ibid.*, p. 3303.
20. V. Müller, H. Zentgraf, I. Eicken, W. Keller, *Science* **201**, 406 (1978).
21. P. Argos, G. C. Ford, M. G. Rossmann, *Acta Crystallogr. Sect. A* **31**, 499 (1975); G. Bricogne, *ibid.* **32**, 832 (1976).
22. We thank W. Saunders for skillful photography and N. Accomando for assistance with the radiography. This work was supported by NSF grant PCM78-17635 to D.L.D.C. from the Human Cell Biology Program and NIH grants CA15468 to D.L.D.C. and CA06654 to W.T.M. from the National Cancer Institute. Requests for reprints should be sent to D.L.D.C.
* Present address: Department of Biochemistry, University of Minnesota Medical Center, Minneapolis 55414.
† Present address: Department of Biophysics, Johns Hopkins University, School of Medicine, Baltimore, Md. 21205.

5 September 1978; revised 30 October 1978

Hybrid Myelomas Producing Antibodies Against a Human Neuroblastoma Antigen Present on Fetal Brain

Abstract. *Spleen cells from mice immunized with a cultured human neuroblastoma were hybridized with the mouse plasmacytoma P3X63Ag8. Hybrid myelomas were screened for production of antibodies that reacted with human neuroblastomas but not with cells from other tissues. One of these hybridoma antibodies reacted with an antigen present on the six human neuroblastomas tested, one of two retinoblastomas, a glioblastoma, and fetal brain, but did not react with other tumors or tissues including adult human brain.*

Production of antiserums against specific antigens on human tumors or tissues has been complicated by the concomitant production of antibodies that react with all human cells. Obtaining antiserum specific for the immunizing cell has required removal of the species-specific antibodies by absorption. Köhler and Milstein (*1, 2*) have introduced methods for producing hybrid myelomas (hybridomas) that synthesize monoclonal antibodies against single antigens, thus circumventing the problem of unwanted antibodies in xenogeneic immunizations (*3-6*). We have developed a hybrid cell line that produces antibodies which react with an antigen present on human neuroblastoma, a retinoblastoma, and fetal brain. A small amount of this antigen is detectable on a glioblastoma, but it is not detectable in significant amounts on other human cell types including adult human brain.

The process of coating human tumor cells with antiserum against another human cell type has been used by other investigators (*7*) to reduce the antibody response against human species antigens and thus increase the specificity against tumor antigens. Antibody-coated cells were employed in our immunization protocol so that fewer hybridoma clones would have to be screened to find those making antibody specific for the human neuroblastomas. The human neuroblastoma line IMR6 (*8*) was incubated with a hyperimmune mouse serum directed against the human lymphoblastoid line 8866. The antibody-coated neuroblastoma cells were washed by centrifugation and injected intraperitoneally into mice. A second injection of coated cells was given intravenously 1 week later; 3 days after the second injection, the spleen cells were removed, made into a single cell suspension, and fused using polyethylene glycol 1000 with the 8-azaguanine-resistant plasmacytoma line P3-X63Ag8. Hybrids grew in HY-HAT medium (*3*) in all the wells of six 96-well plates (Linbro).

Supernatants from 200 wells were tested by microcytotoxicity (*9*) for antibodies against IMR6. Eighty-eight (44 percent) were cytotoxic to IMR6, and 59 (67 percent) of these were not cytotoxic to 8866. The hybrids producing cytotoxic antibody specific for IMR6 were passaged into tissue culture plates with 16-mm wells, and the supernatants were screened for binding to IMR6 and 8866. Antibodies bound to these target cells were detected by ^{125}I-labeled rabbit antibody to the antigen-binding portion of the immunoglobulin (anti-Fab) (*10, 11*). The two hybrids, PI153 and PI125, which showed the highest binding activity to IMR6 with no binding to 8866 were cloned in agarose (*3*), and ten clones of each cell type were analyzed. Supernatants from these 20 clones were assayed for activity against IMR6 and all were positive. The clone from each hybrid line with the highest binding activity was then grown in culture for supernatant collection and passaged as an ascites tumor in pristane-primed mice (*3*). The supernatants from cultures that grew to more than 10^6 cells per milliliter showed binding activity at dilutions of 1/320 or 1/640. All the ascites fluids collected from mice implanted with the cloned hybrids showed binding activity. Ascites PI153/3 exhibited binding activity to a dilution of 1/20,000. The class of antibody produced by the hybridomas

0036-8075/79/0316-1120$00.50/0